Ukrainian Journal of Physical Optics
ISSUE 5
2026

Controllable Localization and Manipulation of Optical Hollow Traps by Means of Optical-Vortex Diffraction

O. Angelsky [1], A. Bekshaev [1,2]*, C. Zenkova [1], I. Mokhun [1], and X. Zhang [3]

[1] Correlation Optics Department, Chernivtsi National University, 2 Kotsyubinsky Str., Chernivtsi 58012, Ukraine
[2] Physics Research Institute, Odesa I.I. Mechnikov National University, 2 V.Zmiienka Str., Odesa 65082, Ukraine,
[3] Nankai University, Tianjin, China
*Corresponding author: bekshaev@onu.edu.ua

Received: 30.08.2026

Abstract. An optical vortex (OV) is coupled with the local intensity zero and is thus a field configuration suitable for "hollow" optical traps and optical tweezers. When an incident circular OV beam experiences diffraction at a rectilinear screen edge (SE), and the SE is far enough from the beam axis, the main consequence is the OV-core displacement from its initial position. Based on the model of an incident Laguerre-Gaussian beam, we investigate analytically and numerically ways to control the OV-core position in the diffracted field by changing the SE position relative to the incident-beam axis. The results show that by regulating the SE position with ~1 μm accuracy, controllable OV-core motion with sub-nanometer accuracy can be realized. We also analyze additional control possibilities related to the incident-beam topological charge, wavefront curvature, SE properties (semitransparent screen, phase-step screen), and the distance between the diffraction plane and the observation plane.

Keywords: Hollow trap, optical tweezer, optical vortex, edge diffraction, vortex-core displacement, controllable manipulation
UDC: 535.4
DOI: 10.3116/16091833/Ukr.J.Phys.Opt.2026.S1003

1. Introduction

Optical tools for trapping and manipulating micro-objects are among the most popular and rapidly developing applications of structured light fields [1,2]. Multiple schemes of optical traps and optical tweezers (OT) are widely used for deliberate capture, prescribed motion, spatial distribution, and allocation of various micro- and nanoparticles [1–11]. Sometimes, 3D OTs are realized that perform the "full" 3D localization of a selected micro-object, but in many cases, an observed particle is always situated, at least approximately, in a single plane determined by the geometry of the sample (cuvette) [11]. Then, this plane can be considered as the transverse (x, y) plane of a light beam propagating in the longitudinal z-direction, and the task of optical manipulation is reduced to the particle's localization within a chosen area of this "target" plane. In such widespread situations, 2D optical traps and OTs are applicable, which employ focused paraxial beams with well-developed transverse inhomogeneity.

In such fields, a suspended micro-object experiences the gradient force action depending on its dielectric properties. A dielectric particle with a refractive index higher than that of the environment tends to be localized at the intensity maximum; in contrast, particles with a small refractive index (e.g., air bubbles, oil droplets, biological cells in water), as well as absorbing ones, concentrate at the intensity minima ("hollow traps"). An additional advantage of these "hollow OTs" [12–14] is the absence of light-induced damage potentially occurring at the intensity maxima, which is especially important for biological and fragile objects. In such situations, the beams with phase singularities (optical vortices, OVs) [15–18] are especially suitable [1,10]. A characteristic feature of such beams is the existence of a phase singularity ("OV core"). It is a point of the beam cross section (x, y) where the field amplitude possesses an isolated zero (a suitable attribute of the hollow trap). Simultaneously, the optical phase experiences an increment of $2\pi m$ on a round trip near the core, m being the integer topological charge of the singularity.

In various OT applications, the crucial issue is the ability to tune and regulate the trap position at the target plane with good thermal, mechanical, and optical stability, along with a suitable and reliable calibration procedure, resulting in high precision and accuracy. Normally, the task of tuning and regulation is fulfilled by a projective optical system including a spatial light modulator followed by the focusing objective with high numerical aperture [3–10]. There are many specific realizations of such an arrangement, but all of them obey similar wave-optics limitations which practically restrict the available accuracy to values of $\sim 0.1\lambda$, where λ is the radiation wavelength [19,20]. In this work, we consider an alternative approach to spatially tuning the hollow OT in the target plane, which exploits the regularities of OV-beam diffraction.

Diffraction is one of the most traditional and extensively studied phenomena in classical optics [19,20]. However, the edge diffraction of circular OV beams [21–34] (see the general scheme in Fig. 1 below) shows many impressive non-trivial details associated with their special physical attributes: helical wavefront shape and transverse energy circulation. In this case, common and well-studied diffraction effects (fringes, transverse diffusion of light energy, etc.) are supplemented by OV-specific transformations of the diffracted beam profile. For the purposes of this paper, the most important diffraction effects appear under conditions of weak diffraction perturbation (WDP), when the screen edge (SE) is located far enough from the incident beam axis. Practically, for usual OV beams, the WDP conditions are realized if the screen is distanced from the axis by two or more beam radii measured at the e^{-1} intensity level, and the diffracted beam profile visually preserves the initial circular shape. Nevertheless, the exact OV position shows dramatic transformations, although on microscopic scales:

(i) In a single-charged circular OV, the OV core displaces from the nominal beam axis; the displacement magnitude and direction depend on the SE position and the post-screen propagation distance z;

(ii) Like due to any breakdown of the OV-beam circular symmetry [35–38], a high-order OV (with the topological charge m, $|m| > 1$) is decomposed into a set of $|m|$ secondary single-charged ones, situated in closely adjacent but different points of the beam cross section, and their positions also evolve with changing the SE position and the post-screen propagation distance;

(iii) At the WDP conditions, when the SE performs a monotonous translation in the transverse direction towards or away from the beam axis [20–22], the perturbed OV cores describe spiral-like trajectories which are very sensitive to the SE position in the transverse plane [29–34].

In particular, the diffraction-induced spiral evolution of the OV cores is one of the most spectacular demonstrations of the rotational properties inherent in the OV beams. On the other hand, the features (i) – (iii) signify that there is a possibility for very fine adjustment of the OV-core position in the diffracted OV beam by means of the rather coarse regulation of the SE location with respect to the incident beam axis. In this paper, we provide a detailed evaluation and numerical characterization of these procedures, keeping in mind the requirements of hollow optical trapping and OT techniques.

We start with a description of the general scheme for the OV-beam diffraction, quantification of the WDP conditions, and presentation of the asymptotic analytical model [29–32] for the diffraction of circular Laguerre-Gaussian (LG) beams [1,15,16] with zero radial index (Section 2). Afterward, the described theoretical tools are applied to analyze the diffracted field and its modifications depending on the SE position relative to the incident-beam axis; the main focus is the behavior of the OV cores, which form the physical essence of the hollow traps. In this view, the single-charged incident OV beams ($|m| = 1$) appear to be the most promising, and examples of possible OV-core trajectories observable at different diffraction configurations are considered in Section 3. Section 4 discusses additional possibilities for controllable OV-core migration that emerge from variations in the incident-beam wavefront. The results are summarized in the Conclusion (Section 5), where their general meaning is discussed, along with possible further practical applications, generalizations, and specifications.

2. Principal scheme of the OV diffraction

A typical arrangement for observation of the OV diffraction [21–34] is presented in Fig. 1a. As a standard example of the "source" OV beam, we consider the circular LG mode [15–18], which can be easily obtained in a laser cavity as well as produced extra-cavity from the circular Gaussian beam. The incident circular OV beam propagates along the z-axis (which is simultaneously its symmetry axis) and passes near the diffraction obstacle S situated in the transverse 'diffraction plane' (x_a, y_a) orthogonal to the propagation axis. The SE is parallel to the axis y_a and can be translated along the direction x_a so that the axes (x_a, y_a, z) form the Cartesian frame (Fig. 1a). The SE position a with respect to the beam axis and the observation-plane position z with respect to the screen plane are precisely adjustable.

Following the usual practice reflected in most previous works [21–27], we consider the incident monochromatic beam (frequency ω, wavenumber $k = \omega / c$, and wavelength $\lambda = 2\pi/k$, c is the light velocity) with a homogeneous linear polarization as a scalar field. Under the paraxial conditions [1,16,18], the beam spatial structure is characterized by the slowly varying complex amplitude $u(x,y,z)$, so that the electric field at any spatial point (x, y, z) at the moment of time t equals to $E = \mathrm{Re}\left[u(x,y,z)\exp(ikz - i\omega t)\right]$. At the diffraction plane ($z = z_a$), the incident beam complex amplitude equals to $u(x_a, y_a, z_a)$, and after passing the screen, it experiences the transformation

$$u_a(x_a, y_a) = T(x_a, y_a)\,u(x_a, y_a, z_a) \tag{1}$$

where $T(x_a, y_a)$ is the spatially inhomogeneous screen transmission coefficient. For the edge diffraction (Fig. 1a), we accept $T(x_a, y_a)$ in the following form:

$$T(x_a, y_a) = \begin{cases} 1, \; x_a < a; \\ \tau, \; x_a \ge a, \end{cases} \tag{2}$$

τ is the complex number characterizing the screen properties. In the usual diffraction case, where the screen is opaque and has a sharp edge, $\tau = 0$, but the form (2) includes the situations of phase-step diffraction $\tau = \exp(i\varphi)$ [33,34] with an arbitrary constant phase shift φ, or a partially transparent screen with $0 < \tau < 1$.

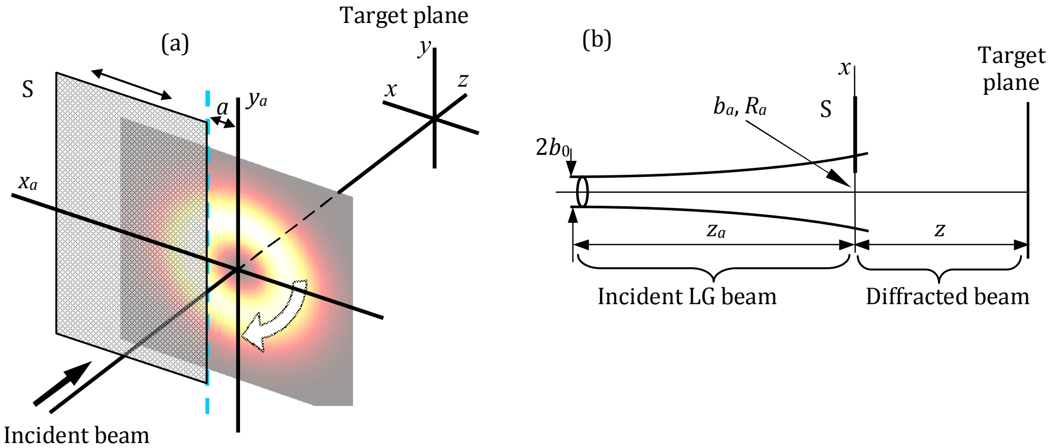

Fig. 1. General scheme of the OV beam diffraction: (a) magnified view of the beam screening and the involved coordinate frames, the white arrow shows the transverse energy circulation in a beam with positive topological charge, $m > 0$; (b) scheme of evolution and diffraction of the incident LG beam: S is the diffraction obstacle (the edge is parallel to axis y, its adjustable position along axis x is characterized by the distance a from the axis z), the diffraction pattern is registered in the observation (target) plane. Further explanations are given in the text.

For simplicity, we restrict the consideration to the incident LG beams with zero radial index; in the resulting LG_{0m} modes, the azimuthal index m coincides with the OV topological charge. For them [18,29,30]

$$u(x_a,y_a,z_a)=\frac{(-i)^{|m|+1}}{\sqrt{|m|!}}\left(\frac{z_R}{z_a-iz_R}\right)^{|m|+1}\left(\frac{x_a+i\sigma y_a}{b_0}\right)^{|m|}\exp\left(\frac{ik}{2}\frac{x_a^2+y_a^2}{z_a-iz_R}\right), \quad (3)$$

where $\sigma=\mathrm{sgn}(m)=\pm 1$, b_0 is the Gaussian envelope waist radius, z_a is the distance from the waist cross-section to the screen plane (see Fig. 1b), and $z_R=kb_0^2$ is the corresponding Rayleigh length. The helical wavefront is described by the term

$$(x_a+i\sigma y_a)^{|m|}=\sqrt{x_a^2+y_a^2}\exp\left(im\arctan\frac{y_a}{x_a}\right), \quad (4)$$

the current beam radius b_a and the curvature radius R_a of the spherical wavefront component in the screen plane are determined by the well-known equations [1,15,18]

$$b_a^2=b_0^2\left(1+\frac{z_a^2}{z_R^2}\right), \quad R_a=z_a+\frac{z_R^2}{z_a}. \quad (5)$$

In the scheme of Fig. 1, the diffracted field at a distance z behind S (target plane in Fig. 1) is described by the Kirchhoff-Fresnel integral [19]

$$u(x,y,z)=\frac{k}{2\pi iz}\int_{-\infty}^{\infty}dy_a\int_{-\infty}^{a}dx_a\,u_a(x_a,y_a)\exp\left\{\frac{ik}{2z}\left[(x-x_a)^2+(y-y_a)^2\right]\right\}. \quad (6)$$

Substitution of Eqs. (1) – (3) into the integral formula (6) gives possibilities for fruitful numerical and analytical investigations of the diffracted field and its relations with the diffraction-scheme parameters. Remarkably, under WDP conditions, the calculations can be performed using the asymptotic analytical model valid for $a >> b_a$ [29–32]. Here, we employ this model and, for simplicity (and, as will be shown below, with no limitation of generality), accept the condition

$$z_a = 0, \tag{7a}$$

which implies

$$b_a = b_0 \,,\; R_a = \infty \,, \tag{7b}$$

(the diffraction plane coincides with the waist plane of the incident beam (3)). In this case, the result of integration (6) in the near-axis region $x << b_a$, $y << b_a$ can be presented in the form

$$u(x,y,z) \simeq Br^{|m|}\exp(im\phi) - D(1-\tau)a^{|m|-1}\exp\left[\frac{ika^2}{2}\left(\frac{i}{z_R}+\frac{1}{z}\right)\right], \tag{8}$$

where $r = \sqrt{x^2 + y^2}$ and $\phi = \arctan(y/x)$ are the polar coordinates in the target plane,

$$B = \frac{1}{(z - iz_R)^{|m|+1}}\,,\quad D = \sqrt{\frac{i}{2\pi}\frac{k}{z}}(-iz_R)^{-|m|-1}\left[k\left(\frac{1}{z}+\frac{i}{z_R}\right)\right]^{-3/2}. \tag{9}$$

Hence, the expressions for the OV cores' polar coordinates can be easily found via equating (8) to zero:

$$\begin{aligned} r &= \left\{a^{|m|-1}\exp\left(-\frac{a^2}{2b_a^2}\right)\left|\frac{D(1-\tau)}{B}\right|\right\}^{1/|m|} \\ &= a^{1-1/|m|}\left[|1-\tau|\exp\left(-\frac{a^2}{2b_a^2}\right)\sqrt{\frac{z}{2\pi k}\sqrt{1+\left(\frac{z}{z_R}\right)^2}}\right]^{1/|m|}, \end{aligned} \tag{10}$$

$$\begin{aligned} \phi + M\cos\phi &= \frac{1}{m}\left\{\arg\left[D(1-\tau)\right] - \arg B\right\} + \frac{ka^2}{2mz} + \frac{2N}{m}\pi \\ &= \frac{\arg(1-\tau)}{m} + \frac{1}{m}\left(|m| - \frac{1}{2}\right)\arctan\left(\frac{z}{z_R}\right) + \frac{\pi}{4m} + \frac{ka^2}{2mz} + \frac{2N}{m}\pi, \qquad N = 0, 1, \ldots |m|-1, \end{aligned} \tag{11}$$

where

$$M = \frac{kra}{mz}\,, \tag{12}$$

and $N+1$ is the "number" of a secondary single-charged OV formed after diffraction (if $|m| = 1$, there is only one OV corresponding to $N = 0$). The results (10) – (12) are valid in the nearest vicinity of the beam axis, $r << b_a$; with this precaution, due to the rapid exponential decay of the field amplitude (3) with increasing off-axial distance a, they offer an approximately 1% accuracy [29–31] for

$$a \gtrsim 2.5 b_a\,. \tag{13}$$

On the other hand, they obey the conditions for the Fresnel-Kirchhoff approximation, which imply that the distances between the involved points of the diffraction plane and of the target plane should be much larger than the diffraction aperture [19,39]. In application to LG beam diffraction, these conditions require

$$\left(\frac{z}{b_a}\right)^3 \gg \frac{kb_a}{16\pi}\,, \tag{14}$$

and, for example, if $kb_a \simeq 10^3$, dictate that the distance between the screen plane and the target plane should not be too small, practically $z \gtrsim 10b_a$. The appropriateness of the model (8) – (12) with provisions (13), (14) has been confirmed by direct numerical calculations of the Fresnel-Kirchhoff integral (6) and in OV-diffraction experiments [29–34].

3. Diffraction-induced motion of the OV core: diffraction at the beam waist

Eqs. (9) – (11) enable us to reveal all the important details of the diffraction-induced migration of the OV cores observable in the target plane. We illustrate this behavior with the help of several examples of diffracted LG modes (3), satisfying the waist-plane conditions (7); for numerical estimations, we accept the beam parameters

$$k = 10^5\ \text{cm}^{-1},\quad b_0 = 0.01\ \text{cm}. \qquad (15)$$

The accepted value of k approximately corresponds to the He-Ne laser radiation, while the waist radius (~100 μm) corresponds to $(kb_0) = 1000$, which warrants the applicability of the paraxial description [1,16]. The distance z to the target plane is selected within the range $2\ \text{cm} < z < 10\ \text{cm}$, while the SE position varies near the value $a \approx 2.5 b_a$. Under these conventions, the requirements (13), (14) are well satisfied, and the formulae (10) – (12) are applicable.

We start with a short comparison of the patterns available at different topological charges of the incident beam. Fig. 2a presents the fragments of the observable OV trajectories for m = 1, 2, and 3 (for beams with opposite signs of m, the trajectories can be obtained via the mirror reflection with respect to the horizontal x-axis [29–32]). The figure shows that the diffraction of an m-charged OV indeed produces $|m|$ single-charged secondary OVs in the diffracted field. They perform seemingly separate evolutions; however, the intensity “barriers” between their cores are rather low at the considered WDP situation. As a result, the optical traps formed, e.g., by the OV cores A, B, and C, originated from the 3-charged incident OV (green curves), are not well isolated from each other, and rather constitute a single “blurred” trap. In Fig. 2b, the trap boundaries are conventionally characterized by the contours corresponding to the intensity level of 5% of the maximum, and the broadening, asymmetry, and deformations of the 2nd- and 3rd-order OV “traps” (red and green lines), in contrast to the 1st-order trap (blue contour), are clearly seen. Of course, such “composite” traps as shown by the red and green lines will be less efficient than the one formed by the “genuine” single-charged OV. Besides, Fig. 2a shows that the same SE increments

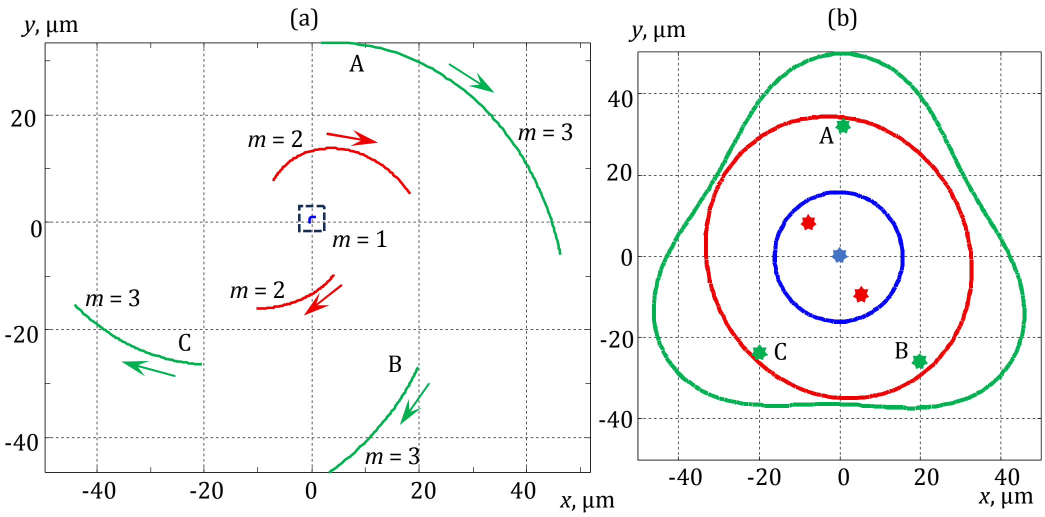

Fig. 2. Characteristics of the OV-core positions and the near-core intensity distributions in the target plane $z = 5$ cm (see Fig. 1) for diffraction at the opaque screen ($\tau = 0$ in Eqs. (10), (11)) of an LG beam (3) with the topological charge: m = 1 (blue); m = 2 (red); m = 3 (green). (a) OV-core trajectories observable when SE translates from $a = 3b_a$ to $a = 2.5b_a$ (the trajectory for m = 1 is shown by the small blue curve inside the dashed square); arrows show the directions of the OV migration. (b) Constant-intensity contours corresponding to 5% of the maximum (calculated from (8), (9)) and the approximate OV-core positions (stars) for $a = 3b_a$ (starting point of the evolution illustrated in (a)). Other explanations are given in the text.

produce much higher displacements of the secondary OVs (red and green curves) than of the "genuine" single-charged OV (the blue curve inside the dashed square near the coordinate origin). This means that the diffraction of a 1st-order OV is much more suitable for fine regulation of the OV-core position via the SE translation. Accordingly, in further consideration, we focus on the case $|m| = 1$ and analyze the situation inside the target plane fragment denoted by the dashed square of Fig. 2a.

Further details relating to the diffracted field of a single-charged incident LG beam (3) are presented in Fig. 3 where additional characteristics of the diffraction-induced OV-core displacements are illustrated. As has been established earlier [29–34], the SE translation induces a spiral-like motion of the OV core in the (x, y)-plane; with growing z, the spiral curvature decreases, and the trajectory 'as a whole' shows a higher deviation from the beam axis (Fig. 3a). Numerical evaluation of the interrelations between the OV position and the SE displacement a can be obtained with the help of Fig. 3b where the a-dependent behavior of the OV-core Cartesian coordinates ($x = r\cos\phi$, $y = r\sin\phi$) is shown (solid lines). Additionally, the derivatives dx/da and dy/da are presented by the dashed curves, which illustrate the sensitivity of the OV-core location to the screen position a (see Fig. 1). According to these data, the SE shift $\Delta a \approx 0.01 b_a = 1$ μm results in the OV-core shift $(|\Delta x|, |\Delta y|) \approx 0.02$ μm. This fact illustrates the general useful regularity: Controlling the SE position with an accuracy δ enables to control the OV localization with the accuracy $\sim 0.02\delta$, and this is obtained from the first occasional example.

Undoubtedly, special efforts to improve accuracy can enhance this evaluation. The simplest ways may be associated with utilization of a semitransparent screen: the data of Fig. 3 are obtained for $\tau = 0$ (see Eq. (2)) whereas, in agreement with Eq. (10) for $|m| = 1$, r is proportional to $(1 - \tau) < 1$, and the absolute values of the controllable OV-core displacement $(|\Delta x|, |\Delta y|)$ can be easily reduced several times for the same Δa, if a screen with $0.5 < \tau < 1$ is used.

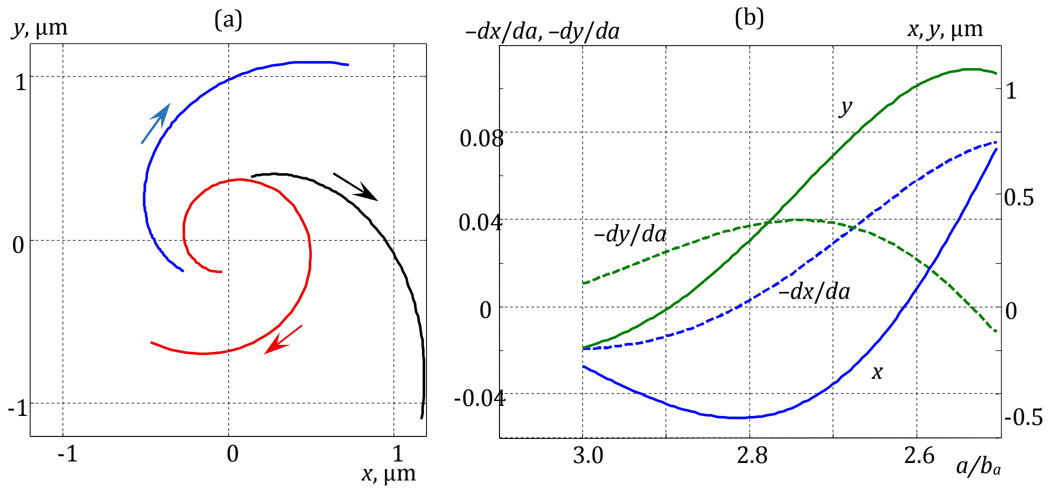

Fig. 3. Characteristics of the diffracted-field OV-core motion for the incident LG_{01} beam (3) with the topological charge $m = 1$ and parameters (7a), (7b), (15), observable when the opaque-screen ($\tau = 0$ in Eqs. (10), (11)) translates from $a = 3b_a$ to $a = 2.5b_a$: (a) OV-core trajectory in the target plane $z = 2$ cm (red line), $z = 5$ cm (blue line) – the same as the blue curve inside the dashed square at the center of Fig. 2a, and $z = 7$ cm (black line); arrows show the directions of the OV motion when the SE moves from the beam periphery towards the axis; (b) a-dependent evolution of the OV-core Cartesian coordinates x, y (solid lines, right scale) and of the derivatives $-dx/da$, $-dy/da$ (dashed lines, left scale) in the target plane $z = 5$ cm. Negative signs of the derivatives reflect that the observed evolution is caused by the SE translation from higher to lower a (note the reverse horizontal scale in (b)).

However, the OV trajectory's high sensitivity to SE position is not the only characteristic important for controllable OT localization. Fig. 3a shows that a simple SE translation induces rather intricate curvilinear OV trajectories whose behavior strongly depends on the post-screen propagation distance z. Generally, this is not a serious defect for possible OV tuning because, in cases of high accuracy, the expected OV-core deviations from the assigned point are so small that the trajectory can be replaced by the rectilinear segment whose direction is dictated by the local values of dx/da, dy/da at this point. Moreover, the dependence of the OV trajectories on z can be used for deliberate assignment of the direction in which the OV moves in response to a certain standard SE displacement. Nevertheless, the search of conditions where the OV core performs a less intricate, more predictable, preferably straight-line trajectories, looks a reasonable task. This can be achieved, e.g., by employing an additional “degree of freedom”, which appears if we remove the restrictions (7) and admit the incident LG beams with spherical wavefronts [30].

4. Description of the OV displacements for the incident LG beam with a spherical wavefront

The above consideration was based on the simplifying assumptions (7), which meant that the incident-beam wavefront curvature is exclusively associated with the helical phase (4) and has no spherical component; upon further discussion, it was emphasized that the conditions (7) imply no limitation of generality. Now we elucidate this argument and use it to analyze the influence of spherical wavefront curvature. To this end, we involve another simple rule for the transformation of the diffracted beam complex amplitude that occurs if the incident beam is modified according to the equation

$$u(x_a, y_a) \to u(x_a, y_a)\exp\left(ik\frac{x_a^2 + y_a^2}{2R_a}\right), \tag{16}$$

(i.e., the spherical wavefront component is added to the beam, preserving the same intensity profile [28]). Practically, the transformation (16) can be realized by a proper spherical lens placed immediately before or behind the diffraction plane. In such a situation, if the initial distribution $u(x_a, y_a)$ (“prototype beam”) produces the diffracted field with complex amplitude $u_p(x, y, z)$, the modified initial beam (16) produces the diffracted field described by

$$u(x,y,z) = \frac{1}{\left(1+\dfrac{z}{R_a}\right)}\exp\left[ik\frac{x^2+y^2}{2(z+R_a)}\right]u_p\left(\frac{x}{\left(1+\dfrac{z}{R_a}\right)}, \frac{y}{\left(1+\dfrac{z}{R_a}\right)}, \frac{z}{\left(1+\dfrac{z}{R_a}\right)}\right), \tag{17}$$

(this can be shown immediately from the Fresnel-Kirchhoff integral (3) [28,30]). To elucidate the meaning of this rule, let us suppose that the incident prototype beam $u(x_a, y_a)$, being diffracted, produces in the cross section z_0 behind the screen such a complex amplitude distribution, for which the OV core is situated at the point ($x = x_0, y = y_0$). Hence, Eq. (17) dictates that the modified incident beam (16) produces the diffracted field in whose cross section

$$z = \frac{z_0}{1 - z_0/R_a}, \tag{18}$$

the OV core is located at the point

$$x = \frac{x_0}{1 - z_0/R_a}, \quad y = \frac{y_0}{1 - z_0/R_a}. \tag{19}$$

In application to Eqs. (9) – (11), this rule yields

$$r = \left[a\left(1 + \frac{z}{R_a}\right) \right]^{1-1/|m|} \left[|1-\tau| \exp\left(-\frac{a^2}{2b_a^2}\right) \sqrt{\frac{z}{2\pi k}\sqrt{\left(1+\frac{z}{R_a}\right)^2 + \left(\frac{z}{z_R}\right)^2}} \right]^{1/|m|}, \tag{20}$$

$$\phi + M\cos\phi = \frac{\arg(1-\tau)}{m} + \frac{1}{m}\left(|m| - \frac{1}{2}\right)\arctan\left[\frac{z}{z_R(1+z/R_a)}\right] + \frac{\pi}{4m} + \frac{ka^2}{2mz} + \frac{ka^2}{2mR_a} + \frac{2N}{m}\pi. \tag{21}$$

In particular, the far field of the diffracted prototype beam is realized in the modified-beam diffraction at

$$z = -R_a. \tag{22}$$

This distance between the diffraction plane and the target plane can be physically realized if $R_a < 0$ (converging wavefront). In fact, this situation occurs if a lens with focal length $f_a = -R_a$ is placed in the diffraction plane and the target plane is assigned at the lens's focal plane; there, the Fraunhofer pattern of the diffracted field is reproduced.

Fig. 4a illustrates this situation, showing several possible OV-core trajectories achievable at the target plane (22) upon diffraction of a single-charge LG mode (3) subjected to transformation (16) with $R_a = -z$. At the standard conditions of an opaque screen ($\tau = 0$ in Eqs. (20), (21)), the spiral-like trajectory of Fig. 3a degenerates into the straight line parallel to the SE (blue lines); in the geometry of Fig. 1, the SE translation from the beam periphery to

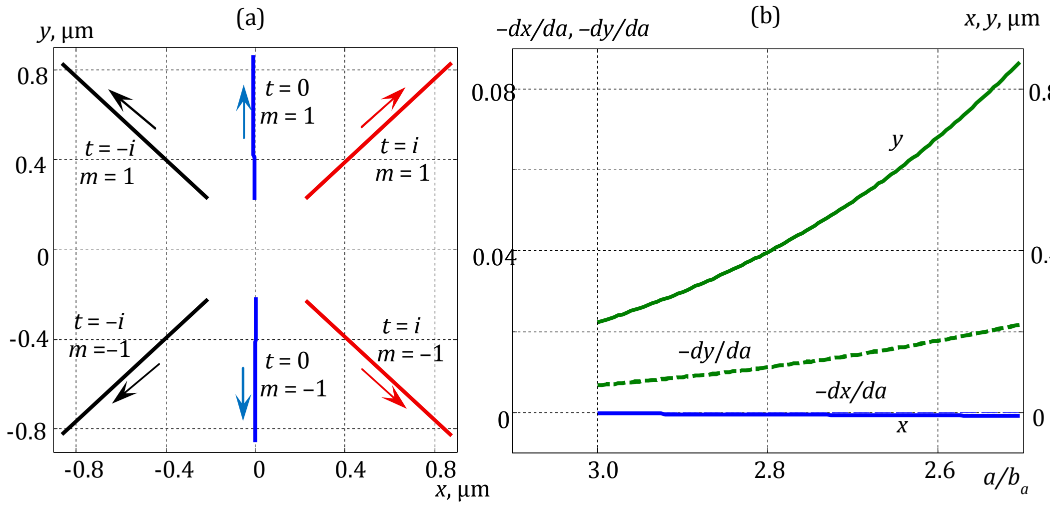

Fig. 4. Characteristics of the OV-core behavior in the diffracted field for the incident LG beam (3) with parameters (7a), (7b), (15), transformed according to Eq. (16) with $R_a = -5$ cm, observable in the target plane $z = 5$ cm while the SE translates from $a = 3b_a$ to $a = 2.5b_a$ (see Fig. 1): (a) OV-core trajectory in the target plane for the screen with $\tau = 0$ (blue), $\tau = \exp(i\pi/2)$ (red), $\tau = \exp(-i\pi/2)$ (black) and for positive ($m = 1$) and negative ($m = -1$) topological charge; arrows show the directions of the OV motion when the SE moves from the beam periphery towards the axis; (b) a-dependent evolution of the OV-core Cartesian coordinates x, y (solid lines, right scale) and of the derivatives $-dx/da$, $-dy/da$ (dashed lines, left scale) for $\tau = 0$ and $m = 1$ (blue graphs for x and dx/da practically do not differ from the horizontal zero-line). Other conventions are as in Fig. 3b.

the axis induces the OV-core motion along the y-axis (at m = 1), and opposite to it (at m = –1). This rectilinear motion is performed almost uniformly, slightly accelerating with decreasing a, as can be seen from the curves of Fig. 4b. The available value of $|dy/da| \approx 0.01$ is even lower than in the case of Fig. 3, enabling the accuracy of the OV-core localization of 0.01δ if the SE position is tuned with accuracy δ. Of course, the possibilities of further improving the accuracy by using a semitransparent screen, discussed in Section 3 and associated with the term $(1 - \tau)$ in Eqs. (20), (21) are equally applicable in this case.

Remarkably, not only are the vertical rectilinear OV trajectories available in the target plane (22). Additional possibilities are coupled with the diffraction at a rectilinear phase step [33,34] realized in the scheme of Fig. 1a if $\tau = \exp(i\varphi)$ in Eq. (2). For example, at $\varphi = \pi/2$, the OV position evolves along the bisectors of the 1st and 4th quadrants, regarding the OV sign, $m = \pm 1$ (red lines in Fig. 4a); at $\varphi = -\pi/2$, the OV moves along the bisectors of the 2nd and 3rd quadrants (black lines). For other phase-step values φ, intermediate OV-core trajectories can be obtained.

5. Conclusion

The examples and calculations considered in the above Sections support the idea that the predictable and controllable adjustment of the OV-core location can be realized in the process of edge diffraction of circular OV-beams (3) under the WDP conditions (13). Besides the controllable OV-core localization, the WDP conditions offer the specific advantage of approximately preserving the initial circular symmetry of the near-core intensity distribution [29–32] (see, for example, the blue equal-intensity contour in Fig. 2b), thus providing appropriate conditions for the usual trapping and manipulating OT functions. The results of this paper illustrate the main principles and testify to their general validity. At the same time, the specific details of the corresponding arrangements and procedures may be modified to suit the specific tasks and requirements.

The above-described examples represent some of the simplest and most evident realizations of the proposed ideas. However, the presented mathematical model, resulting in the main relations (10), (11), (20), and (21), offers a wide range of practical possibilities associated with the proper adjustment of the incident-beam configuration (b_a, R_a) and the diffraction parameters (τ, a, z). With proper selection of the beam structure and diffraction geometry, many specific OV-core trajectories in the diffracted field can be realized, which may be useful for OT assembly and operation, as well as for specific solutions aimed at micro-object allocation and manipulation. In particular, immediate and readily implementable next steps can involve using “complex” semitransparent screens ($\tau = |\tau|\exp(i\varphi)$) with properly adjusted transparency $0 < |\tau| < 1$ and phase-step value φ.

The results presented in Figs. 3 and 4 show that regulation of the SE position with accuracy δ enables control of the OV-core position in the diffracted field (and, consequently, manipulation of the corresponding hollow-trap position) with the accuracy δ/γ where the “accuracy-enhancement coefficient” $\gamma \approx 10^2$. Moreover, the simple considerations involving the semitransparent screen (Section 3) indicate that this value can be easily improved by an order of magnitude, promising $\gamma \approx 10^3$. This means that, for example, SE positioning with 1 μm accuracy, which is achievable with existing mechanical driving tools [3–10], produces impressive OT-localization accuracy of ~1 nm. But this is not the final limit. If necessary (and this is the usual situation), the proposed diffraction scheme of Fig. 1 can certainly be supplemented by an optical projection system which forms the target-plane image with appropriate reduction of the transverse geometric size and proportional enhancement of the OT localization accuracy to the sub-nanometer scale. Additional prospects may be associated with employment of more "gentle" OV-diffraction schemes, e.g., diffraction at a "soft" edge [40].

In conclusion, the incident LG beam model (3) accepted in this paper imposes no principal restrictions, and similar ideas can be applied to other types of OV beams, e.g., Bessel beams, Kummer beams, etc. Bessel beams are widely applicable in OT techniques [13,14]; Kummer-type beams, or "Hypergeometric modes," are produced by widespread tools for OV-beam generation, such as "fork" holograms or spiral phase plates [41–47]. A characteristic feature of such beams is the slower intensity fall-off at the beam periphery: the intensity decays according to a power law instead of exponentially in (3), and the decay is non-monotonous but of oscillatory character. As a consequence, WDP conditions generally occur at higher a than dictated by the exponential model (Eq. (13)); the derivatives of the diffraction-induced OV-core displacement, $|dx/da|$ and $|dy/da|$, are generally higher than presented and discussed in Figs. 3, 4, and the corresponding OV-core trajectories expose small oscillations and seeming irregularities [29,31,32,34]. At first glance, these peculiarities are unfavorable for OT applications; on the other hand, they open many new possibilities that may have practical implementations. If necessary, these and other possible generalizations (for example, those related to the asymmetry of the incident OV beams [36,37]) can be carried out based on the approach formulated and developed in this paper.

On the other hand, keep in mind that the OV-core position is not the only parameter that governs the localization of an OT-trapped object. Its actual place within a hollow-trap area is determined by the complex interrelations between the gradient forces applied to separate parts of the object, which, in turn, are dictated by its size, asymmetry, etc. Additionally, an object may undergo external dynamical influences, from the inertial forces in the case of a non-stationary trap, up to the Brownian motion inside the suspending medium [3–10]. All these complications require special investigations which lie beyond our present scope. Obviously, these factors may reduce the localization accuracy available in practical situations; at the same time, all the possibilities for diffraction-induced purposeful OT positioning considered in the paper remain relevant and applicable regardless of the trapped object's nature. In this context, the accuracy estimates presented in this paper show the theoretical limits of accuracy for diffraction-induced positioning of OV-based OTs.

Funding. This research was supported by the National Research Foundation of Ukraine (NRFU), project No. 2025.06/0086 "Innovative Methods and Systems of Laser Communication in Turbulent Atmospheric Environments Based on Phase Singularities".

Acknowledgments. The authors are grateful to the Department of Correlation Optics at Yuriy Fedkovych Chernivtsi National University for encouraging support of this work.

Disclosures. The authors declare no conflicts of interest.

Authors' contribution. O. Angelsky formulated the idea of controllable displacements of the OV cores in diffraction fields, contributed to the theoretical analysis, participated in the discussion of the obtained results, and contributed to the writing of the article. A. Bekshaev formulated the analytical model for the OV diffraction process, contributed to the numerical calculations, participated in the discussion of the obtained results, and contributed to the writing of the article. C. Zenkova participated in the numerical calculations, contributed to the discussion of the obtained results, and contributed to the writing of the article. I. Mokhun proposed the idea of regulating the OV trajectories via the wavefront curvature of the input beam, participated in the numerical calculations, contributed to the discussion of the obtained results, and contributed to the writing of the article. X. Zhang participated in the analytical calculations, contributed to the discussion of the obtained results, and contributed to the writing of the article.

References

1. Angelsky, O. V., Bekshaev, A. Y., Hanson, S. G., Zenkova, C. Y., Mokhun, I. I. & Zheng, J. (2020). Structured light: Ideas and concepts. *Front. Phys., 8*, 114.
2. Rubinsztein-Dunlop, H., Forbes, A., Berry, M. V., Dennis, M. R., Andrews, D. L., et al. (2017). Roadmap on structured light. *J. Opt.*, *19*, 013001.
3. Padgett, M. J., Molloy, J., & McGloin, D., editors. (2010). Optical Tweezers: Methods and applications. *CRC press*.
4. Dholakia, K., MacDonald, M., & Spalding, G. (2002). Optical tweezers: the next generation. *Physics World, 15*(10), 31–35.
5. Molloy, J. E. & Padgett, M. J. (2002). Lights, action: Optical tweezers. *Contemporary Physics, 43*(4), 241–258.
6. Nieminen, T. A., Knöner, G., Heckenberg, N. R., & Rubinsztein-Dunlop, H. (2007). Physics of optical tweezers. *Methods in Cell Biology, 82*, 207–236.
7. Moffitt, J. R., Chemla, Y. R., Smith, S. B., & Bustamante, C. (2008). Recent advances in optical tweezers. *Annu. Rev. Biochem., 77*(1), 205–228.
8. Polimeno, P., Magazzu, A., Iati, M. A., Patti, F., Saija, R., Boschi, C. D. E. et al. (2018). Optical tweezers and their applications. *J. Quant. Spectrosc. Radiat. Transfer, 218*, 131–150.
9. Pesce, G., Jones, P. H., Maragò, O. M. & Volpe, G. (2020). Optical tweezers: theory and practice. *The European Physical Journal Plus, 135*(12), 949.
10. Volpe, G., Maragò, O. M., Rubinsztein-Dunlop, H., Pesce, G., Stilgoe, A. B. et al. (2023). Roadmap for optical tweezers. *J. Phys.: Photonics, 5*(2), 022501.
11. Angelsky, O. V., Zenkova, C. Y., Hanson, S. G., Ivansky, D. I., Tkachuk, V. M., & Zheng, J. (2021). Random object optical field diagnostics by using carbon nanoparticles. *Opt. Express, 29*, 916–928.
12. Pan, Y. L., Kalume, A., Lenton, I. C., Nieminen, T. A., Stilgoe, A. B., Rubinsztein-Dunlop, H., et al. (2019). Optical-trapping of particles in air using parabolic reflectors and a hollow laser beam. *Opt. Express, 27,* 33061–33069.
13. Eckerskorn, N., Li, L., Kirian, R. A., Küpper, J., DePonte, D. P., Krolikowski, W., Lee, W. M., Chapman, H. N., & Rode, A. V. (2013). Hollow Bessel-like beam as an optical guide for a stream of microscopic particles. *Opt. Express, 21*(25), 30492–30499.
14. Zhang, Y., Su, W., Qin, Y., Jin, W., Liu, J., Zhang, M., et al. (2024). Minimum-thermal-disturbance nanoparticle fiber optical tweezers using high-order Bessel-like hollow beam. *Journal of Lightwave Technology, 42*(20), 7336–7341.
15. Soskin, M. S. & Vasnetsov, M. V. (2001). Singular optics. *Prog. Opt.*, *42*, 219–276.
16. Bekshaev, A. Y., Soskin, M. S., & Vasnetsov, M. V. (2008). Paraxial Light Beams with Angular Momentum. *Nova Science Publishers*, *New York*.
17. Dennis, M. R., O'Holleran, K., & Padgett, M. J. (2009). Singular optics: optical vortices and polarization singularities. *Prog. Opt.*, *53*, 293–364.
18. Bekshaev, A. Y., Bliokh, K. Y., & Soskin, M. S. (2011). Internal flows and energy circulation in light beams. *J. Opt.*, *13*, 053001.
19. Born, M., & Wolf, E. (1999). Principles of Optics. *Cambridge University Press, Cambridge*.
20. Solimeno, S., Crosignani, B., & DiPorto, P. (1986). Guiding, Diffraction and Confinement of Optical Radiation. *Academic Press*.
21. Marienko, I. G., Vasnetsov, M. V., & Soskin, M. S. (1999). Diffraction of optical vortices. *Proc. SPIE*, *3904*, 27–34.
22. Vasnetsov, M. V., Marienko, I. G., & Soskin, M. S. (2000). Self-reconstruction of an optical vortex. *JETP Lett.*, *71*, 130–133.

23. Arlt, J. (2003). Handedness and azimuthal energy flow of optical vortex beams. *J. Mod. Opt.*, *50*, 1573–1580.
24. Gorshkov, V. N., Kononenko, A. N., & Soskin, M. S. (2001). Diffraction and self-restoration of a severe screened vortex beam. *Proc. SPIE, 4403*, 127–137.
25. Masajada, J. (2000). Gaussian beams with optical vortex of charge 2- and 3- diffraction by a half-plane and slit. *Optica Applicata, 30*, 248–256.
26. Masajada, J. (2000). Half-plane diffraction in the case of Gaussian beams containing an optical vortex. *Opt. Commun.*, *175*, 289–294.
27. Cui, H. X., Wang, X. L., Gu, B., Li, Y. N., Chen, J., & Wang, H. T. (2012). Angular diffraction of an optical vortex induced by the Gouy phase. *J. Opt.*, *14,* 055707.
28. Bekshaev, A. Y., Mohammed. K. A., & Kurka, I. A. (2014). Transverse energy circulation and the edge diffraction of an optical-vortex beam. *Appl. Opt.*, *53*, B27–B37.
29. Bekshaev, A. Y., Chernykh, A,, Khoroshun, A, & Mikhaylovskaya, L. (2016). Localization and migration of phase singularities in the edge-diffracted optical-vortex beams. *J. Opt.*, *18*, 024011.
30. Bekshaev, A. Y., Chernykh, A., Khoroshun. A., & Mikhaylovskaya, L (2017) Displacements and evolution of optical vortices in edge-diffracted Laguerre-Gaussian beams. *J. Opt.*, *19*, 055605.
31. Bekshaev, A. Y., Chernykh, A., Khoroshun, A., & Mikhaylovskaya, L. (2017) Singular skeleton evolution and topological reactions in edge-diffracted circular optical-vortex beams. *Opt. Commun. 397*, 72–83.
32. Bekshaev, A. Y., Angelsky, O. V., & Hanson, S. G. (2018). Transformations and evolution of phase singularities in diffracted optical vortices. In: Advances in Optics: Reviews (vol 1), ed. S. Y. Yurish *International Frequency Sensor Association (IFSA), Barcelona, Spain*. Ch 13, 345–389. (ISBN: 978-84-697-9435-7, e-ISBN: 978-84-697-9436-4)
33. Bekshaev, A. Y., Khoroshun, A, & Mikhaylovskaya, L. (2019). Transformation of the singular skeleton in optical-vortex beams diffracted by a rectilinear phase step. *J. Opt.*, *21*, 084003
34. Bekshaev, A. Y., Chernykh, A., Khoroshun, A., Masajada, J., Popiołek-Masajada, A. & Riazantsev, A. (2021). Controllable singular skeleton formation by means of the Kummer optical-vortex diffraction at a rectilinear phase step. *J. Opt., 23*, 034002.
35. Freund, I. (1999). Critical point explosions in two-dimensional wave fields. *Opt. Commun*. *159*(1), 99–117.
36. Bekshaev, A. Y., Soskin, M. S., & Vasnetsov, M. V. (2004). Transformation of higher-order optical vortices upon focusing by an astigmatic lens. *Opt. Commun.*, *241*, 237–247.
37. Bekshaev, A. Y., & Karamoch, A. I. (2008). Astigmatic telescopic transformation of a high-order optical vortex. *Opt. Commun.*, *281*, 5687–5696.
38. F. Ricci, F., Löffler, W., & van Exter, M. P. (2012). Instability of higher-order optical vortices analyzed with a multi-pinhole interferometer. *Opt. Express. 20*(20), 22961–22975.
39. Masatsugu Sei Suzuki. Kirchhoff-Fresnel Diffraction https://ru.scribd.com/document/817997107/LN-15S-Fresnel-diffraction (accessed 09.07.2026)
40. Bekshaev, A. Y,, & Mikhaylovskaya, L. (2019). Displacements of optical vortices in Laguerre–Gaussian beams diffracted by a soft-edge screen. *Opt. Commun.*, *447*, 80–88.
41. Kotlyar, V. V., Skidanov, R. V., Khonina, S. N., & Balalayev, S. A. (2006). Hypergeometric modes. *Computer Optics*, *30*, 16-22.
42. Kotlyar, V. V., Kovalev, A. A., Skidanov, R. V., Khonina, S. N., & Turunen, J. (2008). Generating hypergeometric laser beams with a diffractive optical element. *Appl. Opt.*, *47*(32), 6124-6133.
43. Karimi, E., Zito, G., Piccirillo, B., Marrucci, L., & Santamato, E. (2007). Hypergeometric-gaussian modes. *Opt. Lett.*, *32*(21), 3053-3055.
44. Bekshaev, A. Y., & Karamoch, A. I. (2008). Spatial characteristics of vortex light beams produced by diffraction gratings with embedded phase singularity. *Opt. Commun.*, *281*, 1366–1374.
45. Bekshaev, A. Y., Orlinska, O., & Vasnetsov, M. V. (2010). Optical vortex generation with a "fork" hologram under conditions of high-angle diffraction. *Opt. Commun.*, *283*, 2006–2016.
46. Bekshaev. A. Y., & Karamoch, A. I. (2008). Displacements and deformations of a vortex light beam produced by the diffraction grating with embedded phase singularity. *Opt. Commun., 281*, 3597–3610.
47. Khonina, S. N., Ustinov, A. V., Logachev, V. I., & Porfirev, A. P. (2020). Properties of vortex light fields generated by generalized spiral phase plates. *Phys. Rev. A*, *101*(4), 043829.

Angelsky, O., Bekshaev, A., Zenkova, C., Mokhun, I., & Zhang, X. (2026). Controllable Localization and Manipulation of Optical Hollow Traps by Means of Optical-Vortex Diffraction. *Ukrainian Journal of Physical Optics*, *27*(5), S1003 – S1016.
doi: 0.3116/16091833/Ukr.J.Phys.Opt.2026.S1003

Анотація. *Оптичний вихор (ОВ) супроводжується локальним нулем інтенсивності й, таким чином, є конфігурацією поля, придатною для «порожнистих» оптичних пасток та оптичних пінцетів. Коли вхідний циркулярний ОВ-пучок зазнає дифракції на прямолінійному краї екрана (КЕ), і КЕ знаходиться достатньо далеко від осі пучка, основним наслідком дифракції є зсув ядра ОВ відносно його початкового положення. На основі моделі вхідного лагерр-гауссового пучка аналітично та чисельно досліджуються способи керування положенням ядра ОВ у дифрагованому полі шляхом зміни положення КЕ відносно осі вхідного пучка. Результати показують, що регулювання положення КЕ з точністю ~1 мкм дозволяє реалізувати керований рух ядра ОВ з субнанометровою точністю. Аналізуються додаткові можливості керування, пов'язані з топологічним зарядом вхідного пучка, кривизною хвильового фронту, властивостями КЕ (напівпрозорий екран, екран зі зміною фази) та відстанню між площиною дифракції та площиною спостереження.*

Ключові слова: *Порожниста пастка, оптичний пінцет, оптичний вихор, крайова дифракція, зсув ядра вихору, кероване пересування.*